Modelling Simul. Mater. Sci. Eng. **16** (2008) 055005 (26pp) doi:10.1088/0965-0393/16/5/055005

A discrete dislocation–transformation model for austenitic single crystals

J Shi[1], S Turteltaub[1], E Van der Giessen[2] and J J C Remmers[1,3]

[1] Faculty of Aerospace Engineering, Delft University of Technology, Kluyverweg 1, 2629 HS Delft, The Netherlands
[2] Zernike Institute for Advanced Materials, University of Groningen, Nijenborgh 4, 9747 AG Groningen, The Netherlands

E-mail: {J.Shi,S.R.Turteltaub}@tudelft.nl and E.van.der.Giessen@rug.nl

Received 4 February 2008, in final form 27 May 2008
Published 19 June 2008
Online at stacks.iop.org/MSMSE/16/055005

Abstract
A discrete model for analyzing the interaction between plastic flow and martensitic phase transformations is developed. The model is intended for simulating the microstructure evolution in a single crystal of austenite that transforms non-homogeneously into martensite. The plastic flow in the untransformed austenite is simulated using a plane-strain discrete dislocation model. The phase transformation is modeled via the nucleation and growth of discrete martensitic regions embedded in the austenitic single crystal. At each instant during loading, the coupled elasto-plasto-transformation problem is solved using the superposition of analytical solutions for the discrete dislocations and discrete transformation regions embedded in an infinite homogeneous medium and the numerical solution of a complementary problem used to enforce the actual boundary conditions and the heterogeneities in the medium. In order to describe the nucleation and growth of martensitic regions, a nucleation criterion and a kinetic law suitable for discrete regions are specified. The constitutive rules used in discrete dislocation simulations are supplemented with additional evolution rules to account for the phase transformation. To illustrate the basic features of the model, simulations of specimens under plane-strain uniaxial extension and contraction are analyzed. The simulations indicate that plastic flow reduces the average stress at which transformation begins, but it also reduces the transformation rate when compared with benchmark simulations without plasticity. Furthermore, due to local stress fluctuations caused by dislocations, martensitic systems can be activated even though transformation would not appear to be favorable based on the average stress. Conversely, the simulations indicate that the plastic hardening behavior is influenced by the reduction in the effective austenitic grain size due to the

[3] Current address: Eindhoven University of Technology, PO Box 513, WH, 5600 MB Eindhoven, The Netherlands.

evolution of transformation. During cyclic simulations, the coupled plasticity-transformation model predicts plastic deformations during unloading, with a significant increase in dislocation density. This information is relevant for the development of meso- and macroscopic elasto-plasto-transformation models.

(Some figures in this article are in colour only in the electronic version)

1. Introduction

Martensitic carbon steels are known to achieve high levels of strength although they tend to have a low ductility, which often makes them unsuitable for applications where formability is important. In order to take advantage of the strength of the martensitic phase while preserving good formability, new classes of low-alloyed multiphase carbon steels have been developed. The microstructure of these steels is typically composed of isolated grains of the retained austenite embedded in a ferritic matrix [1–4]. Upon subsequent mechanical deformation (e.g. during forming), the grains of retained austenite might partially or totally transform into martensite and the strength of the material is increased. Inside carbon-rich austenitic grains, the martensite appears in the form of plate-like regions. Kinematically, the transformation is characterized by a combination of a simple shear and a volumetric expansion, which needs to be accommodated by plastic deformations in the surrounding phases (i.e. untransformed austenite and ferrite), a phenomenon usually referred to as transformation-induced plasticity.

Traditionally, a distinction is made between the so-called stress-induced transformation, where the austenite deforms only elastically prior to transformation, and the so-called strain-assisted transformation, where plastic deformation in the austenite precedes the martensitic transformation. In a sense, neither term is comprehensive since the two phenomena are coupled and their evolution is complex, without a necessarily clear distinction between cause and effect. Nonetheless, the interaction between martensitic transformations and plasticity is of paramount importance in order to understand the mechanisms that control the overall properties of these steels, i.e. ductility and strength.

Modeling of transformation-induced plasticity is an area of active research [5–15]. Nevertheless, a detailed understanding of this fundamental interaction is still far from complete. Macro- and mesoscopic models for transformation-induced plasticity are based on purely phenomenological plasticity theories or, at best, on a crystal plasticity approach. These methods offer the advantages of continuum models, but the interaction between phase transitions and plasticity is simplified through an implicit 'smearing-out' of both phenomena. Such approaches are unable to pick up the interaction between unit transformation events and the dislocation plasticity taking place at the submicrometer length scale. In particular, freshly transformed martensitic plates create new obstacles for the dislocation glide and significantly modify the local stress fields, which affect the evolution of the plastic deformation. These effects are not taken into account in phenomenological plasticity models.

In this contribution, a model based on discrete dislocation plasticity and discrete transformation regions is proposed in order to study the small-scale interaction between transformation and plasticity in a single crystal grain of austenite. In this approach, the nucleation and evolution of dislocations and martensitic regions are modeled explicitly (i.e. without internal variables). The goals of this contribution are to (i) quantify the influence of the martensitic regions on the nature and extent of the plastic deformation in the untransformed austenite and (ii) determine the effect of the induced dislocations on further nucleation of martensite. This information can be used to develop more accurate meso- and macroscopic models. Furthermore, although this work focuses on mechanically induced martensitic transformations, the results of these simulations are of direct relevance for dual steels as well as for maraging steels due to the correspondence between thermally induced and mechanically induced martensite.

The paper is organized as follows: the basic constitutive models for transformation and plasticity and the procedure to solve the (instantaneous) transformation-plasticity problem are developed in section 2. Additional constitutive information to determine the evolution of transformation and plastic flow is presented in section 3. Numerical examples of uniaxial extension and contraction and loading/unloading cycles are given in section 4 to study the interaction between plastic deformations and phase transformations. Concluding remarks are presented in section 5. As a general scheme of notation, scalars are written as lightface italic letters, vectors as boldface lowercase letters (e.g. $\boldsymbol{a}$, $\boldsymbol{b}$) and second-order tensors as boldface capital letters (e.g. $\boldsymbol{A}, \boldsymbol{B}$) except for the stress and strain tensors for which boldface Greek letters are used. Fourth-order tensors are denoted using blackboard bold capital letters (e.g. $\mathbb{A}$, $\mathbb{B}$). The action of a second-order tensor upon a vector is denoted as $\boldsymbol{A}\,\boldsymbol{b}$ (in components $A_{ij}b_j$ with implicit summation on repeated indices) and the action of a fourth-order tensor upon a second-order tensor is written as $\mathbb{A}\boldsymbol{B}$ (i.e. $A_{ijkl}B_{kl}$). The composition of two fourth-order tensors is denoted as $\mathbb{A}\,\mathbb{B}$ (i.e. $A_{ijkl}B_{klmn}$). The tensor product between two vectors is denoted as $\boldsymbol{a}\otimes\boldsymbol{b}$ (i.e. a_ib_j) and between two second-order tensors as $\boldsymbol{A}\otimes\boldsymbol{B}$ (i.e. $A_{ij}B_{kl}$). All inner products are indicated by a single dot between tensorial quantities of the same order (e.g. $\boldsymbol{a}\cdot\boldsymbol{b}$ and $\boldsymbol{A}\cdot\boldsymbol{B}$, i.e. a_ib_i and $A_{ij}B_{ij}$). Super- and subscript indices are typically used to refer to discrete entities (e.g. martensitic plates or dislocations). Additional notation is introduced where required.

2. The instantaneous state of a body undergoing phase transformation and plastic deformation

2.1. Basic assumptions and overview of the method

We consider a single crystal specimen that occupies a region Ω with boundary $\partial\Omega$. The specimen is subjected to prescribed displacements $\boldsymbol{u}_0 = \boldsymbol{u}_0(\boldsymbol{x}, t)$ for points $\boldsymbol{x}$ on one part of the boundary (denoted as $\partial\Omega_u$) and to prescribed tractions $\boldsymbol{t}_0 = \boldsymbol{t}_0(\boldsymbol{x}, t)$ on the complementary part of the boundary (denoted as $\partial\Omega_t$). It is assumed that the loading process occurs quasi-statically, so that at each instant t an equilibrium problem is solved for a given configuration of the specimen. Suppose that the specimen is initially in a stress-free austenitic phase and contains no mobile dislocations. As the specimen is loaded, it may deform plastically and/or transform into martensite.

In particular, as illustrated in figure 1, suppose that at time t the specimen contains $N^{\mathrm{m}} = N^{\mathrm{m}}(t)$ martensitic plates (represented by dark gray regions) and $N^{\mathrm{d}} = N^{\mathrm{d}}(t)$ dislocations (represented by the symbols $\perp$ and $\top$ along a slip line for positive and negative dislocations). In order to determine the displacement $\boldsymbol{u}$, strain ε and stress $\boldsymbol{\sigma}$ fields, the problem is decomposed into three subproblems, namely, that of (i) martensitic plates in an infinite austenitic medium, (ii) dislocations in an infinite homogeneous medium (either austenite or martensite) and (iii) a complementary problem in a finite, heterogeneous medium that contains austenite and martensite (see figure 1). Consequently, the stress, strain and displacement fields of the original problem can be expressed as, respectively,

$$\boldsymbol{\sigma} = \boldsymbol{\sigma}^{\mathrm{m}} + \boldsymbol{\sigma}^{\mathrm{d}} + \boldsymbol{\sigma}^{\mathrm{c}}, \tag{1}$$

$$\varepsilon = \varepsilon^{\mathrm{m}} + \varepsilon^{\mathrm{d}} + \varepsilon^{\mathrm{c}}, \tag{2}$$

$$\boldsymbol{u} = \boldsymbol{u}^{\mathrm{m}} + \boldsymbol{u}^{\mathrm{d}} + \boldsymbol{u}^{\mathrm{c}}, \tag{3}$$

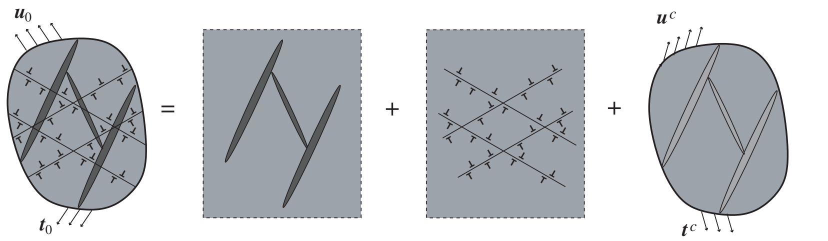

Figure 1. Schematic illustration of the method.

where the superscripts m, d and c refer to the solutions of the transformation, dislocation and complementary problems, respectively. In subproblem (i) each martensitic plate k (with $k = 1, \ldots, N^{\mathrm{m}}$) is taken to be embedded in an infinite homogeneous *austenitic* matrix. In subproblem (ii), each dislocation i (with $i = 1, \ldots, N^{\mathrm{d}}$) is taken to be in an infinite austenitic matrix (respectively, martensitic matrix) if the core of the dislocation is in the austenitic region (respectively, martensitic region) at time t. Hence, more precisely, subproblems (i) and (ii) correspond, respectively, to a collection of N^{m} and N^{d} individual problems and the total transformation and dislocation fields are defined as the summation of the contributions of the individual martensitic plates and dislocations, i.e.

$$\boldsymbol{\sigma}^{\mathrm{m}} := \sum_{k=1}^{N^{\mathrm{m}}} \boldsymbol{\sigma}_k^{\mathrm{m}}, \qquad \boldsymbol{\sigma}^{\mathrm{d}} := \sum_{i=1}^{N^{\mathrm{d}}} \boldsymbol{\sigma}_i^{\mathrm{d}}\,, \tag{4}$$

$$\boldsymbol{\varepsilon}^{\mathrm{m}} := \sum_{k=1}^{N^{\mathrm{m}}} \boldsymbol{\varepsilon}_k^{\mathrm{m}}, \qquad \boldsymbol{\varepsilon}^{\mathrm{d}} := \sum_{i=1}^{N^{\mathrm{d}}} \boldsymbol{\varepsilon}_i^{\mathrm{d}}, \tag{5}$$

$$\boldsymbol{u}^{\mathrm{m}} := \sum_{k=1}^{N^{\mathrm{m}}} \boldsymbol{u}_k^{\mathrm{m}}, \qquad \boldsymbol{u}^{\mathrm{d}} := \sum_{i=1}^{N^{\mathrm{d}}} \boldsymbol{u}_i^{\mathrm{d}}\,, \tag{6}$$

where quantities with subscripts k or i refer to the individual fields of a martensitic plate k or a dislocation i. It is important to note that since the fields associated with individual martensitic plates and dislocations are obtained in an infinite homogeneous matrix, neither the boundary conditions of the original problem nor the heterogeneities of the matrix are accounted for. Consequently, the complementary field is introduced in order to satisfy the boundary conditions of the original problem as well as the equilibrium equation in a nonhomogeneous domain composed of austenitic and martensitic regions.

The transformation and dislocations fields can be determined analytically whereas the complementary field is computed numerically. It is worth mentioning that in the discrete dislocation method presented by Van der Giessen and Needleman [16], the purpose of the decomposition of the actual field into a dislocation and complementary fields was to avoid, in the numerical solution, the singular fields related to dislocations. In the present context, since the stress field related to the appearance of a martensitic plate is not singular, in principle it may be combined with the complementary field. Nonetheless, the decomposition given in (1) is useful since the stress field related to a martensitic plate can be determined analytically for evolving martensitic plates, as discussed in the subsequent section, and thus avoids a computationally costly re-meshing procedure to preserve the same degree of accuracy. Furthermore, accuracy at the interface between the austenite and martensite is important to determine the evolution of the martensitic plates.

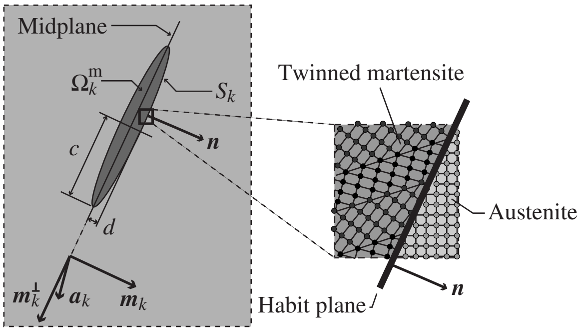

Figure 2. Martensitic plate (with an internally twinned structure) in an austenitic matrix.

2.2. *Stress field associated with a martensitic plate in an infinite austenitic matrix*

2.2.1. Transformation kinematics. In this model, attention is restricted to thin-plate twinned martensite as a product phase. This type of martensite has relatively straight interfaces with the adjacent (untransformed) austenite and a fairly uniform twinned internal substructure. The transformation is characterized crystallographically as a change from a face centered cubic (FCC) austenitic lattice to twin-related body centered tetragonal (BCT) martensitic lattices. For a cubic to tetragonal change, the unconstrained theory of martensitic transformations indicates that there are 24 possible crystallographically distinct arrangements of twinned martensite that form coherent interfaces with austenite. Each possible arrangement consists of alternating layers of two twin-related martensitic BCT variants with specific orientations and proportions (see the inset in figure 2 for an illustration of an arrangement of twinned martensite). Crystallographically distinct arrangements of twinned martensite are characterized by a pair of vectors $\{\boldsymbol{a}, \boldsymbol{m}\}$ and, in analogy to slip systems, this pair of vectors is referred to as a *transformation system*. The vector $\boldsymbol{a}$ is the average transformation shape vector of the two twin-related variants of martensite and $\boldsymbol{m}$ is the normal vector to the austenite–martensite interface, known as the *habit plane*, under *unconstrained* conditions (i.e. for average stress-free conditions). From the theory of martensitic transformations and within the framework of small deformations, the change in shape during an unconstrained transformation from austenite into twinned martensite is characterized by a transformation strain tensor $\varepsilon_k^{\mathrm{tr}}$ that can be expressed as (see, e.g. [17–19])

$$\varepsilon_k^{\mathrm{tr}} := \frac{1}{2}\left(\boldsymbol{a}_k \otimes \boldsymbol{m}_k + \boldsymbol{m}_k \otimes \boldsymbol{a}_k\right) , \tag{7}$$

where the subscript k refers to the kth martensitic plate. At the scale of observation considered in this model, only one transformation system is allowed to occupy a given region (i.e. martensitic platelets are assumed to be composed of a single transformation system). Consequently, the vectors $\{\boldsymbol{a}_k, \boldsymbol{m}_k\}$ correspond to the characteristic vectors of the specific system (among the crystallographically distinct systems) that became active in that region during loading. In addition, the crystallographic characteristics of twinned martensite under constrained conditions (e.g. a martensitic plate fully surrounded by an austenitic matrix) are assumed to be the same as in the unconstrained case; hence, the model does not take into account possible detwinning.

In this model, the specimen is assumed to be under plane-strain conditions perpendicular to and loaded in the $(1\,1\,0)_{\mathrm{a}}$ plane, where the subscript indicates that the Miller indices are referred to the FCC austenitic lattice. This orientation is often adopted in planar discrete dislocation simulations in order to interpret plastic slip as being generated by the movement of pure edge dislocation in an FCC lattice (see, e.g. [20]). However, in a typical FCC to BCT transformation, the experimentally observed as well as the theoretically computed vectors $\boldsymbol{a}_k$ and $\boldsymbol{m}_k$ are not perpendicular to the out-of-plane $[1\,1\,0]_{\mathrm{a}}$ direction. Nonetheless, in order to keep the formulation consistent with plane-strain conditions, the transformation systems considered in the present analysis are assumed such that the habit plane normal and the shape strain vector are perpendicular to the out-of-plane direction of the specimen. Similar to the approach used for slip systems under plane-strain conditions, a reduced number of transformation systems is considered (in the present context, only two crystallographically distinct systems will be used).

The in-plane cross-section of a region that transforms into martensite is approximated as an ellipse and the lengths of the semi-axes are denoted by c and d, as shown in figure 2. This choice is motivated by the geometrical resemblance of an elliptical shape to the experimentally observed shapes of martensitic plates at the relevant length scale and by the availability of an analytical solution of the transformation problem for this particular shape. It is noted that, in the absence of external loads and internal constraints, the theory of martensitic transformations predicts that the interface between austenite and martensite is planar (i.e. the vector $\boldsymbol{m}_k$ is constant for all points on the interface). However, under constrained conditions (i.e. when the martensitic plate is embedded in an austenitic matrix), the actual habit plane is not flat. Since the geometrical interpretation of $\boldsymbol{m}_k$ as the habit plane normal is limited to unconstrained transformations, the vector $\boldsymbol{m}_k$ is henceforth referred to as the *unconstrained* habit plane normal (under average stress-free conditions), to distinguish it from the actual habit plane normal $\boldsymbol{n}$ under constrained conditions. The relation between the unconstrained and the constrained habit planes is taken such that the (constant) vector $\boldsymbol{m}_k$ is oriented perpendicularly to the major semi-axis of the ellipse (i.e. midplane of the ellipse, see figure 2).

The transformation strain $\varepsilon_k^{\mathrm{tr}}$ in a martensitic plate k is interpreted as an expansion of magnitude δ in the direction perpendicular to the unconstrained habit plane and a simple shear of magnitude γ parallel to the unconstrained habit plane (symmetrized for consistency with small strain theory), with $\delta = \boldsymbol{a}_k \cdot \boldsymbol{m}_k$ and $\gamma = \boldsymbol{a}_k \cdot \boldsymbol{m}_k^{\perp}$ (no sum on k), where $\boldsymbol{m}_k^{\perp}$ is a unit vector along the unconstrained habit plane. In accordance with the assumptions for the transformation systems, the in-plane transformation strain, referred to the habit plane basis, is given by

$$\varepsilon_k^{\mathrm{tr}} = \tfrac{1}{2}\gamma\,(\boldsymbol{m}_k^{\perp} \otimes \boldsymbol{m}_k + \boldsymbol{m}_k \otimes \boldsymbol{m}_k^{\perp}) + \delta\,(\boldsymbol{m}_k \otimes \boldsymbol{m}_k)\ . \tag{8}$$

2.2.2. Transformation stress field in an infinite medium. As indicated in $(4)_1$, the stress field $\boldsymbol{\sigma}^{\mathrm{m}}$ in an infinite domain due to martensitic transformations is defined as the sum of the stress fields $\boldsymbol{\sigma}_k^{\mathrm{m}}$ caused by individual martensitic plates $k = 1, \ldots, N^{\mathrm{m}}$, each in an infinite austenitic medium (i.e. without taking into account the finiteness of the domain or the mutual interactions between plates). To determine each stress field $\boldsymbol{\sigma}_k^{\mathrm{m}}$, consider an isolated plate Ω_k^{m} of martensite embedded in an infinite austenitic medium $\mathbb{R}^2 - \Omega_k^{\mathrm{m}}$. Let $\mathbb{C}^{\mathrm{a}}$ and $\mathbb{C}^{\mathrm{m}}$ be the tensors of elastic moduli of the austenitic matrix and the martensitic plates, respectively. For the isotropic case,

$$\mathbb{C}^p = \tfrac{1}{3}(3\kappa^p - 2\mu^p)\boldsymbol{I} \otimes \boldsymbol{I} + 2\mu^p \mathbb{I}, \tag{9}$$

where the phase p is either $p = \mathrm{a}$ for austenite or $p = \mathrm{m}$ for martensite, κ^p is the bulk modulus of phase p, μ^p is the shear modulus of phase p and $\boldsymbol{I}$ and $\mathbb{I}$ are the second and fourth-order identity tensors, respectively. The stress field $\boldsymbol{\sigma}_k^{\mathrm{m}}$ is generated due to the imposition of a uniform transformation strain $\varepsilon_k^{\mathrm{tr}}$ inside the plate Ω_k^{m} (i.e. the so-called eigenstrain). The constitutive relations are as follows:

$$\boldsymbol{\sigma}_k^{\mathrm{m}} := \begin{cases} \mathbb{C}^{\mathrm{a}}\varepsilon_k^{\mathrm{m}} & \text{in } \mathbb{R}^2 - \Omega_k^{\mathrm{m}}\ , \\ \mathbb{C}^{\mathrm{m}}\left(\varepsilon_k^{\mathrm{m}} - \varepsilon_k^{\mathrm{tr}}\right) & \text{in } \Omega_k^{\mathrm{m}}. \end{cases} \tag{10}$$

The strain field $\varepsilon_k^{\mathrm{m}}$ and the stress field $\boldsymbol{\sigma}_k^{\mathrm{m}}$ can be computed using the so-called equivalent inclusion method [21]. According to this method, the strain and the stress *inside* the martensitic plate k can be expressed as

$$\varepsilon_k^{\mathrm{m}} = \mathbb{S}\left[\left(\mathbb{C}^{\mathrm{m}} - \mathbb{C}^{\mathrm{a}}\right)\mathbb{S} + \mathbb{C}^{\mathrm{a}}\right]^{-1}\mathbb{C}^{\mathrm{m}}\varepsilon_k^{\mathrm{tr}} \qquad \text{in } \Omega_k^{\mathrm{m}}, \tag{11}$$

$$\boldsymbol{\sigma}_k^{\mathrm{m}} = \mathbb{C}^{\mathrm{a}}\left(\mathbb{S} - \mathbb{I}\right)\left[\left(\mathbb{C}^{\mathrm{m}} - \mathbb{C}^{\mathrm{a}}\right)\mathbb{S} + \mathbb{C}^{\mathrm{a}}\right]^{-1}\mathbb{C}^{\mathrm{m}}\varepsilon_k^{\mathrm{tr}} \qquad \text{in } \Omega_k^{\mathrm{m}}, \tag{12}$$

where $\mathbb{S}$ is Eshelby's tensor (see, e.g. [21]). In the present plane-strain formulation, Eshelby's tensor can be formally obtained from the three-dimensional formulation as the limiting case of an ellipsoidal plate that is infinitely long in the out-of-plane direction. Observe that, since the transformation strain tensor $\varepsilon_k^{\mathrm{tr}}$ is uniform inside the plate, the strain and the stress tensors in the martensitic plate are uniform.

In principle, the stress field $\boldsymbol{\sigma}_k^{\mathrm{m}}$ outside a martensitic plate Ω_k^{m} can be obtained from Eshelby's solution for exterior points using the given transformation strain. However, these formulae are cumbersome in practice and, instead, an alternative method is used to evaluate the stress field for points in $\mathbb{R}^2 - \Omega_k^{\mathrm{m}}$. To this end, observe that the boundary value problem for $\boldsymbol{\sigma}_k^{\mathrm{m}}$ for points outside the martensitic plate (under-plane strain conditions) corresponds to a situation where the domain $\mathbb{R}^2 - \Omega_k^{\mathrm{m}}$ with elastic moduli $\mathbb{C}^{\mathrm{a}}$ is subjected to zero stress at infinity and a traction $\hat{\boldsymbol{t}} = \boldsymbol{\sigma}^{\mathrm{b}}\boldsymbol{n}$ applied on the boundary $S_k = \partial\Omega_k^{\mathrm{m}}$, where $\boldsymbol{\sigma}^{\mathrm{b}}$ is equal to the (constant) stress tensor $\boldsymbol{\sigma}_k^{\mathrm{m}}$ obtained from the interior solution given in (12) and $\boldsymbol{n}$ is the outward normal unit vector on S_k. By superposition, the solution to this boundary value problem can be decomposed as the sum of the solutions to two auxiliary problems: (i) an infinite domain containing a stress-free void Ω_k^{m} and subject to a stress $-\boldsymbol{\sigma}^{\mathrm{b}}$ at infinity and (ii) an infinite medium loaded with a stress $\boldsymbol{\sigma}^{\mathrm{b}}$ at infinity (whose solution is trivially a uniform field $\boldsymbol{\sigma}^{\mathrm{b}}$). The solution to the void problem (i), denoted as $\boldsymbol{\sigma}^{\mathrm{v}}$, can be obtained with the help of Mushkelishvili's potentials that provide the stress, strain and displacement fields of an infinite domain with a stress-free elliptical void under loading at infinity. For brevity, the resulting formulae are not reported here, but for completeness the method is outlined in appendix A.

In summary, the stress field due to a martensitic plate k in an infinite austenitic medium is obtained as

$$\boldsymbol{\sigma}_k^{\mathrm{m}} = \begin{cases} \mathbb{C}^{\mathrm{a}}\left(\mathbb{S} - \mathbb{I}\right)\left[\left(\mathbb{C}^{\mathrm{m}} - \mathbb{C}^{\mathrm{a}}\right)\mathbb{S} + \mathbb{C}^{\mathrm{a}}\right]^{-1}\mathbb{C}^{\mathrm{m}}\varepsilon_k^{\mathrm{tr}} & \text{in } \Omega_k^{\mathrm{m}}, \\ \boldsymbol{\sigma}^{\mathrm{v}} + \mathbb{C}^{\mathrm{a}}\left(\mathbb{S} - \mathbb{I}\right)\left[\left(\mathbb{C}^{\mathrm{m}} - \mathbb{C}^{\mathrm{a}}\right)\mathbb{S} + \mathbb{C}^{\mathrm{a}}\right]^{-1}\mathbb{C}^{\mathrm{m}}\varepsilon_k^{\mathrm{tr}} & \text{in } \mathbb{R}^2 - \Omega_k^{\mathrm{m}}, \end{cases} \tag{13}$$

with the transformation strain $\varepsilon_k^{\mathrm{tr}}$ being given by equation (8). This tensor, together with the elastic properties of the phases and the geometrical characteristics of the martensitic plates which determine the Eshelby tensor, allows the analytical computation of the transformation stress field from (13) and the formulae derived from (A.2) in appendix A.

2.3. *Stress field of discrete dislocations*

Analytical expressions for the displacement $\boldsymbol{u}_i^{\mathrm{d}}$, strain $\varepsilon_i^{\mathrm{d}}$ and stress $\boldsymbol{\sigma}_i^{\mathrm{d}}$ associated with an edge dislocation i in an infinite, isotropic and homogeneous medium are well known and can be found, e.g. in [16]. Since the stress field is singular at the dislocation core, the analytical solution is only used outside the core, which in the present model is defined as a circular region with a radius equal to twice the magnitude of the Burgers vector. Experimental observations indicate that in the martensite that was generated from high-carbon austenite (e.g. more than 1.4 wt% C), the deformation is essentially elastic up to fracture, which can occur at high axial stresses (∼2–4 GPa, see [4,22]). Under these circumstances, the plastic deformation is limited to the austenitic phase, but the martensitic phase can inherit the dislocations generated in the austenitic phase prior to transformation [23]. For simplicity, it is assumed that the strain tensor for dislocations that get trapped in the martensite upon transformation remains the same as in the parent austenitic phase. For isotropic elasticity, the assumption that $\varepsilon_i^{\mathrm{d}}$ remains unchanged upon transformation corresponds to a situation where (i) the Burgers vector remains unchanged after transformation and (ii) Poisson's ratio of the parent and product phases is the same. As shown in section 4.1, the relation between the stiffness of austenite and martensite is such that condition (ii) is satisfied. However, condition (i) implies that the present method does not take into account the change in the Burgers vector due to the change in the lattice structure upon transformation [23]. Nevertheless, a correction in the self-energy of dislocations due to the phase change is performed at the level of the stress tensor, which accounts for the stiffness of the martensitic phase according to the following constitutive relations:

$$\boldsymbol{\sigma}_i^{\mathrm{d}} := \begin{cases} \mathbb{C}^{\mathrm{a}}\varepsilon_i^{\mathrm{d}} & \text{for } i \in \mathcal{A}^{\mathrm{a}} , \\ \mathbb{C}^{\mathrm{m}}\varepsilon_i^{\mathrm{d}} & \text{for } i \in \mathcal{A}_k^{\mathrm{m}},\ k = 1, \ldots, N^{\mathrm{m}} , \end{cases} \tag{14}$$

where $\mathcal{A}^{\mathrm{a}}$ and $\mathcal{A}_k^{\mathrm{m}}$ refer to, respectively, the set of dislocations in the austenitic region Ω^{a} and the set of dislocations in a martensitic plate Ω_k^{m}.

2.4. *Complementary field*

The complementary field is used to satisfy the actual boundary conditions and to account for the inhomogeneities due to the formation of martensitic plates. To this end, observe that the original problem can be expressed as

$$\mathrm{div}\boldsymbol{\sigma} = \mathbf{0} \qquad \text{in } \Omega^* , \tag{15}$$

where the stress–strain relation is given by

$$\boldsymbol{\sigma} = \begin{cases} \mathbb{C}^{\mathrm{a}}\boldsymbol{\varepsilon} & \text{in } \Omega^{\mathrm{a}*} , \\ \mathbb{C}^{\mathrm{m}}\left(\boldsymbol{\varepsilon} - \boldsymbol{\varepsilon}_k^{\mathrm{tr}}\right) & \text{in } \Omega_k^{\mathrm{m}*}, \quad k = 1, \ldots, N^{\mathrm{m}} , \end{cases} \tag{16}$$

and the strain–displacement relation is expressed as

$$\boldsymbol{\varepsilon} = \tfrac{1}{2}\left(\nabla\boldsymbol{u} + \nabla\boldsymbol{u}^{\mathrm{T}}\right) \qquad \text{in } \Omega^* . \tag{17}$$

In equations (15)–(17), Ω^*, $\Omega^{\mathrm{a}*}$ and $\Omega_k^{\mathrm{m}*}$, with $k = 1, \ldots, N^{\mathrm{m}}$, refer to the corresponding domains Ω, Ω^{a} and Ω_k^{m} but excluding the dislocation cores. The boundary conditions are as specified in section 2.1. In view of the decompositions (1)–(6), and the constitutive relations (10) and (14), the complementary boundary value problem is, from (15) to (17), formulated as

$$\mathrm{div}\boldsymbol{\sigma}^{\mathrm{c}} = \mathbf{0} \qquad \text{in } \Omega^*; \tag{18}$$

$$\boldsymbol{\sigma}^{\mathrm{c}} := \begin{cases} \mathbb{C}^{\mathrm{a}}\boldsymbol{\varepsilon}^{\mathrm{c}} + \boldsymbol{P}_{\mathrm{a}}^{\mathrm{d}} & \text{in } \Omega^{\mathrm{a}*}, \\ \mathbb{C}^{\mathrm{m}}\boldsymbol{\varepsilon}^{\mathrm{c}} + \boldsymbol{P}_k^{\mathrm{m}} + \boldsymbol{P}_k^{\mathrm{d}} & \text{in } \Omega_k^{\mathrm{m}*}, \quad k = 1, \ldots, N^{\mathrm{m}}, \end{cases} \tag{19}$$

$$\boldsymbol{\varepsilon}^{\mathrm{c}} = \tfrac{1}{2}\left(\nabla\boldsymbol{u}^{\mathrm{c}} + \left(\nabla\boldsymbol{u}^{\mathrm{c}}\right)^{\mathrm{T}}\right) \qquad \text{in } \Omega^*. \tag{20}$$

In (19), the tensors $\boldsymbol{P}_{\mathrm{a}}^{\mathrm{d}}$, $\boldsymbol{P}_k^{\mathrm{m}}$ and $\boldsymbol{P}_k^{\mathrm{d}}$ are polarization stresses that result from the difference in elastic properties between the austenite and martensite, given by

$$\boldsymbol{P}_{\mathrm{a}}^{\mathrm{d}} := \left(\mathbb{C}^{\mathrm{a}} - \mathbb{C}^{\mathrm{m}}\right) \sum_{j \in \mathcal{A}^{\mathrm{m}}} \boldsymbol{\varepsilon}_j^{\mathrm{d}} \qquad \text{in } \Omega^{\mathrm{a}*}, \tag{21}$$

$$\boldsymbol{P}_k^{\mathrm{m}} := \left(\mathbb{C}^{\mathrm{m}} - \mathbb{C}^{\mathrm{a}}\right) \sum_{l=1, l\neq k}^{N^{\mathrm{m}}} \boldsymbol{\varepsilon}_l^{\mathrm{m}} \qquad \text{in } \Omega_k^{\mathrm{m}*}, \quad k = 1, \ldots, N^{\mathrm{m}}, \tag{22}$$

$$\boldsymbol{P}_k^{\mathrm{d}} := \left(\mathbb{C}^{\mathrm{m}} - \mathbb{C}^{\mathrm{a}}\right) \sum_{j \in \mathcal{A}^{\mathrm{a}}} \boldsymbol{\varepsilon}_j^{\mathrm{d}} \qquad \text{in } \Omega_k^{\mathrm{m}*}, \quad k = 1, \ldots, N^{\mathrm{m}}. \tag{23}$$

The subscripts a and k in (21)–(23) indicate that the polarization stresses are used to correct for the proper stiffness in the austenitic or martensitic regions, respectively, while the superscripts m and d indicate that the polarization stresses are related to the martensitic transformation or the dislocation field, respectively. The set $\mathcal{A}^{\mathrm{m}}$ refers to the set of dislocations in all martensitic plates while, as indicated in section 2.3, $\mathcal{A}^{\mathrm{a}}$ indicates the set of all dislocations in the austenitic region.

The boundary conditions for the complementary problem are as follows: tractions $\boldsymbol{t}^{\mathrm{c}}$ and displacements $\boldsymbol{u}^{\mathrm{c}}$ are prescribed as

$$\boldsymbol{\sigma}^{\mathrm{c}}\boldsymbol{n} = \boldsymbol{t}^{\mathrm{c}} := \boldsymbol{t}_0 - \boldsymbol{t}^{\mathrm{m}} - \boldsymbol{t}^{\mathrm{d}} \qquad \text{on } \partial\Omega_t \;, \tag{24}$$

$$\boldsymbol{u}^{\mathrm{c}} := \boldsymbol{u}_0 - \boldsymbol{u}^{\mathrm{m}} - \boldsymbol{u}^{\mathrm{d}} \qquad \text{on } \partial\Omega_u \;, \tag{25}$$

where $\boldsymbol{n}$ is the outward normal unit vector to $\partial\Omega$ and

$$\boldsymbol{t}^{\mathrm{m}} = \boldsymbol{\sigma}^{\mathrm{m}}\boldsymbol{n}, \qquad \boldsymbol{t}^{\mathrm{d}} = \boldsymbol{\sigma}^{\mathrm{d}}\boldsymbol{n}.$$

Equations (18)–(25) constitute a linear elastic boundary value problem that can be solved numerically for the complementary field. It is worth mentioning that, for the finite element implementation of the complementary problem, a distinction has to be made between the (evolving) austenitic and martensitic regions in order to assign the corresponding stiffnesses and polarization stresses, which in principle should be done using re-meshing or an equivalent technique. For simplicity however, a 'diffuse interface' approach is taken on a fixed mesh, where weighted stiffnesses and polarization stresses are used in elements that are partly austenite and partly martensite, according to a volume average. Nonetheless, since the main contribution to the stress jump across an interface is computed analytically using the field $\boldsymbol{\sigma}^{\mathrm{v}}$ (see (13)), the diffuse interface approach is a reasonable compromise between computational cost and accuracy. For the special case in which the austenitic and martensitic stiffnesses are equal, the stress jump is *completely* determined from the analytical solution given in (13) and all polarization stresses vanish.

The superposition (1)–(3) of the martensitic, dislocation and complementary fields determines the solution to the original problem at a given instant t. The evolution of the state of the material (i.e. the number and location of martensitic plates and dislocations) is specified using a separate set of constitutive rules.

3. Constitutive rules for the evolution of discrete phase transformation and plastic deformation

After determining the (instantaneous) state of a body undergoing phase transformations and plastic deformations, the configuration is updated to account for nucleation and/or growth of martensitic regions and nucleation and/or movement of dislocations. The method is explicit in the sense that the configuration at time $t + \Delta t$ (martensitic regions and dislocations) is determined based on the state at time t.

3.1. Transformation driving force

The nucleation and growth of martensitic domains are treated in this work based on the framework developed by Abeyaratne and Knowles [24, 25] for moving interfaces. Consider a martensitic plate Ω_k^{m} with boundary S_k^{m}. Within the context of small deformations, the transformation driving force at a point on S_k^{m} is given by (see [24])

$$f_k^{\mathrm{tr}} := \rho\, [\![\psi]\!] - \langle \boldsymbol{\sigma} \rangle \boldsymbol{n} \cdot [\![\varepsilon]\!]\, \boldsymbol{n} \qquad \text{on } S_k^{\mathrm{m}}, \tag{26}$$

where ψ is the Helmholtz energy per unit mass, ρ is the mass density and $[\![\psi]\!] := \psi^+ - \psi^-$ is the jump in ψ across the interface, in which ψ^+ and ψ^- represent the limiting values of ψ on S_k^{m} from the austenitic and martensitic sides, respectively. Moreover, $\langle\boldsymbol{\sigma}\rangle := (1/2)\left(\boldsymbol{\sigma}^+ + \boldsymbol{\sigma}^-\right)$ corresponds to the average stress across the interface, where $\boldsymbol{\sigma}^+$ and $\boldsymbol{\sigma}^-$ are the stress tensors on the austenitic and martensitic sides of the interface, respectively. Similarly, $[\![\varepsilon]\!] := \varepsilon^+ - \varepsilon^-$ indicates the jump in strain across the interface. Note that the tensors $\boldsymbol{\sigma}^{\pm}$ refer to the total stress; hence, they include the contributions from the transformation, dislocation and complementary fields, including the transformation field connected to the martensitic plate where the driving force is computed. Furthermore, observe that the (infinitesimal) strain tensor ε is used in (26) instead of the deformation gradient for consistency with the assumptions used in section 2.2.

Under quasi-static conditions, the traction is continuous across the interface with unit normal vector $\boldsymbol{n}$, i.e.

$$\boldsymbol{\sigma}^+\boldsymbol{n} = \boldsymbol{\sigma}^-\boldsymbol{n}; \tag{27}$$

however, the stress tensor is in general not continuous across the interface, i.e. $\boldsymbol{\sigma}^+ \neq \boldsymbol{\sigma}^-$, even if the austenite and martensite have the same stiffnesses.

Since plastic slip is represented by discrete dislocations, the Helmholtz energy refers to the elastic strain energy (i.e. the defect energy is implicitly accounted for in ψ via the elastic deformation associated with the dislocation fields away from the dislocation cores). Consequently, consistent with the constitutive relations (16), the Helmholtz energy can be expressed as

$$\rho\psi := \begin{cases} \frac{1}{2}\varepsilon\cdot\mathbb{C}^{\mathrm{a}}\varepsilon & \text{in } \Omega^{\mathrm{a}*}, \\ \frac{1}{2}\left(\varepsilon - \varepsilon_k^{\mathrm{tr}}\right)\cdot\mathbb{C}^{\mathrm{m}}\left(\varepsilon - \varepsilon_k^{\mathrm{tr}}\right) & \text{in } \Omega_k^{\mathrm{m}*},\ k = 1,\ldots,N^{\mathrm{m}}, \end{cases} \tag{28}$$

where the domains $\Omega^{\mathrm{a}*}$ and $\Omega_k^{\mathrm{m}*}$ exclude the dislocation cores. For simplicity, it is assumed that dislocation cores are not exactly on the surface S_k^{m}, but that the distance from the core to the interface is at least six times the magnitude of the Burgers vector.

It is convenient to express the jump in Helmholtz energy $\rho\,[\![\psi]\!]$ across an interface directly in terms of the stress tensor since the contribution from the transformation field is readily available in terms of stresses (see (13)). Inverting the constitutive laws in the austenitic and martensitic sides of the interface, one has

$$\varepsilon^+ = \mathbb{D}^{\mathrm{a}}\boldsymbol{\sigma}^+, \qquad \varepsilon^- - \varepsilon_k^{\mathrm{tr}} = \mathbb{D}^{\mathrm{m}}\boldsymbol{\sigma}^-, \tag{29}$$

where $\mathbb{D}^{\mathrm{a}} = (\mathbb{C}^{\mathrm{a}})^{-1}$ and $\mathbb{D}^{\mathrm{m}} = (\mathbb{C}^{\mathrm{m}})^{-1}$ are the compliance tensors of the austenite and martensite, respectively. For the isotropic case, $\mathbb{D}^p = (1/3)((3\kappa^p)^{-1} - (2\mu^p)^{-1})\boldsymbol{I}\otimes\boldsymbol{I} + (2\mu^p)^{-1}\mathbb{I}$, with phase p representing austenite ($p = \mathrm{a}$) or martensite ($p = \mathrm{m}$). Making use of the constitutive relations (16) and in view of (28) and (29), the jump in Helmholtz energy across the interface is given by

$$\rho\,[\![\psi]\!] = \tfrac{1}{2}\boldsymbol{\sigma}^+\cdot\mathbb{D}^{\mathrm{a}}\boldsymbol{\sigma}^+ - \tfrac{1}{2}\boldsymbol{\sigma}^-\cdot\mathbb{D}^{\mathrm{m}}\boldsymbol{\sigma}^-. \tag{30}$$

If the elastic strains in the austenitic and martensitic sides of the interface are small in comparison with the transformation strain, the jump in the strain tensor can be approximated by (minus) the transformation strain, i.e.

$$[\![\varepsilon]\!] \approx -\varepsilon_k^{\mathrm{tr}}. \tag{31}$$

Making use of (27), (30) and (31) and rearranging the order of terms, the driving force defined in (26) can be written as

$$f_k^{\mathrm{tr}} \approx \boldsymbol{\sigma}^{\pm}\boldsymbol{n}\cdot\varepsilon_k^{\mathrm{tr}}\boldsymbol{n} + \tfrac{1}{2}\mathbb{D}^{\mathrm{a}}\boldsymbol{\sigma}^+\cdot\boldsymbol{\sigma}^+ - \tfrac{1}{2}\mathbb{D}^{\mathrm{m}}\boldsymbol{\sigma}^-\cdot\boldsymbol{\sigma}^- \qquad \text{on } S_k^{\mathrm{m}}, \tag{32}$$

with $\varepsilon_k^{\mathrm{tr}}$ given by (7) for the specific transformation system that nucleated in platelet k. For the computation of the driving force, the actual habit plane normal $\boldsymbol{n}$ has to be employed instead of the unconstrained habit plane normal $\boldsymbol{m}_k$ in order to take into account the curvature of the martensitic plate, particularly at the tips of the elliptical cross-section where $\boldsymbol{m}_k$ and $\boldsymbol{n}$ are perpendicular to each other.

3.2. Nucleation of martensitic plates and transformation kinetic law

To describe the onset and evolution of martensitic transformations, a nucleation criterion and kinetic law need to be specified. In the present model, nucleation (point) sources are randomly distributed in the material. At each source, all transformation systems are monitored for possible nucleation and the most favorable is allowed to nucleate. To this end, prior to nucleation, the driving force is estimated at each nucleation point k and for each crystallographically distinct transformation system based only on the first term of the driving force (32) for an ideally flat interface that coincides with the corresponding unconstrained habit plane, i.e.

$$f_k^{\mathrm{nuc}} := \boldsymbol{\sigma} \cdot \varepsilon_k^{\mathrm{tr}} = \boldsymbol{\sigma} \cdot (\boldsymbol{a}_k \otimes \boldsymbol{m}_k)\,. \tag{33}$$

A potentially active system is chosen when the maximum driving force exceeds a local critical value $f_k^{\mathrm{cr}} > 0$, i.e.

$$f_k^{\mathrm{nuc}} \geqslant f_k^{\mathrm{cr}}\,. \tag{34}$$

If the maximum nucleation driving force corresponds to more than one system, then a potentially active system is randomly chosen among the maximally loaded systems. Subsequently, the possible growth of an embryonic martensitic plate of semi-axes c_0 and d_0 and centered at the source k is tested. The potentially active crystallographic system is temporarily assigned as the system that appears in the embryonic plate k. The final criterion to allow the actual nucleation of an embryonic plate is that it can grow, based on the growth criterion introduced below. If the plate is allowed to nucleate, the system $\{\boldsymbol{a}_k, \boldsymbol{m}_k\}$ is permanently assigned to the plate and the source is removed from the set of transformation sources. Embryonic plates that cannot grow are not allowed to nucleate; the source is monitored for possible nucleation during later times.

Subsequent to the precipitation of a small embryonic plate, growth is assumed to occur by the lateral movement of the tips of the elliptical cross-section (i.e. in the direction of $\pm\boldsymbol{m}_k^{\perp}$, along a line that passes through the nucleation point). In the present model, it is assumed that the aspect ratio $e := d/c$ of the martensitic plates is preserved during growth. The locations of the tips (which are labeled as 1 and 2, see figure 3) together with the aspect ratio e are sufficient to completely specify the shape of the plate at any time t. Consequently, the growth of a plate can be specified in terms of the velocities of the tips, which are denoted as $v_{\mathrm{t}}^{(1)}$ and $v_{\mathrm{t}}^{(2)}$ and are taken as positive (growth in both directions). Within the framework of irreversible thermodynamics, the evolution of the phase transformation is determined by a kinetic relation (constitutive relation) between an affinity (the driving force) and a flux (rate of transformation). The product of the affinity and the flux is equal to the dissipation due to the transformation. Following this approach, kinetic relations for moving austenite–martensite interfaces $S_k^{\mathrm{m}} = S_k^{\mathrm{m}}(t)$ are often specified as constitutive relations between the value of the driving force $f_k^{\mathrm{tr}}(\boldsymbol{x})$ and the normal velocity $V_{\mathrm{n}}(\boldsymbol{x})$ of the interface at a point $\boldsymbol{x} \in S_k^{\mathrm{m}}$. In general, the transformation driving force f_k^{tr} given by (32) varies along the interface since the stress field is not uniform. Consequently, an ellipse will not retain its shape during growth for homogeneous kinetic relations (such as a linear relation between f_k^{tr} and V_{n}). Accordingly, instead of specifying a pointwise growth relation for the interface, an 'effective' evolution law is proposed for lateral growth such that (i) the total dissipation corresponds to the sum of the local dissipations as the interface moves and (ii) the aspect ratio is kept constant. The goal is

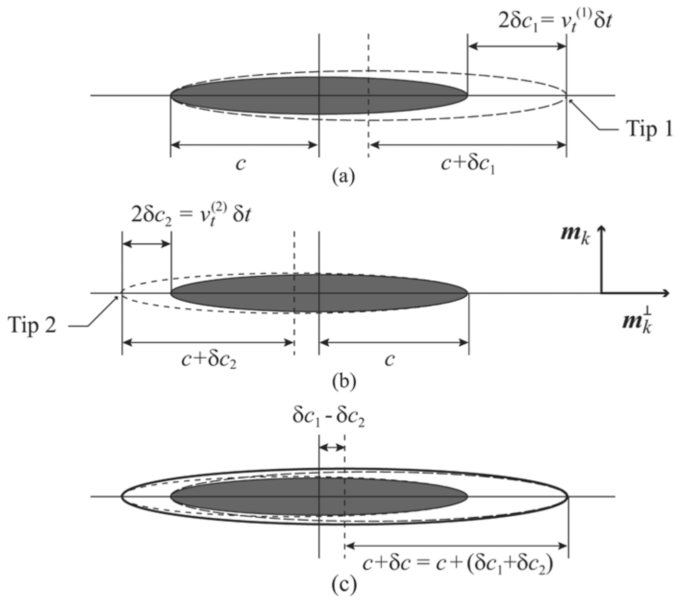

Figure 3. Growth of an elliptical martensitic plate: (*a*) growth due to movement of tip 1; (*b*) growth due to tip 2; (*c*) combined growth, at a constant aspect ratio.

to find a relation between the tip velocities and an effective driving force while satisfying the conditions (i) and (ii). To this end, let $\mathcal{D}_k^{(q)}$ be the total dissipation due to the movement of tip q while the opposite tip is held fixed (see figure 3(*a*) for $q = 1$ and figure 3(*b*) for $q = 2$). In each case, the total dissipation is obtained from the local contributions at each point on the interface, i.e.

$$\mathcal{D}_k^{(q)} := \int_{S_k^{\mathrm{m}}} f_k^{\mathrm{tr}} V_{\mathrm{n}}^{(q)}\,\mathrm{d}s \qquad (q = 1, 2), \tag{35}$$

where $V_{\mathrm{n}}^{(q)} = V_{\mathrm{n}}^{(q)}(\boldsymbol{x})$ is the normal velocity of the interface during lateral growth. If tip q is allowed to move while the opposite tip is held fixed, then the normal velocity $V_{\mathrm{n}}^{(q)}$ can be expressed as

$$V_{\mathrm{n}}^{(q)}(\boldsymbol{x}) = w^{(q)}(\boldsymbol{x})v_{\mathrm{t}}^{(q)} \qquad (q = 1, 2), \tag{36}$$

where $w^{(1)}$ and $w^{(2)}$ are weighting functions that are independent of $v_{\mathrm{t}}^{(1)}$ and $v_{\mathrm{t}}^{(2)}$. For brevity, the expressions for the weighting functions $w^{(1)}$ and $w^{(2)}$ are not shown here, but can be obtained by differentiating the equation of an ellipse with respect to the location of one tip. The function $w^{(1)}$, as seen in figure 3(*a*), is equal to 1 at tip 1 and decays monotonically to 0 at tip 2 as $\boldsymbol{x}$ varies along either side of the perimeter of the elliptical cross-section. The weighting function $w^{(2)}$ is a mirror image of $w^{(1)}$ about the minor semi-axis of the elliptical cross-section (see figure 3(*b*)). Using (36) in (35) provides the following expression for the dissipation:

$$\mathcal{D}_k^{(q)} = \left(\int_{S_k^{\mathrm{m}}} f_k^{\mathrm{tr}} w^{(q)}\,\mathrm{d}s\right) v_{\mathrm{t}}^{(q)} \qquad (q = 1, 2). \tag{37}$$

The kinetic relation used in the present model for the lateral growth of a plate is expressed in terms of an effective driving force $\bar{f}_k^{(q)}$ and the rate of change in the cross-sectional area of the martensitic plate Ω_k^{m}. The effective driving force is defined such that the dissipation is given by

$$\mathcal{D}_k^{(q)} = \bar{f}_k^{(q)} \frac{\mathrm{d}}{\mathrm{d}t} \left(\Omega_k^{\mathrm{m}}\right)^{(q)}, \tag{38}$$

where $(\mathrm{d}/\mathrm{d}t)\left(\Omega_k^{\mathrm{m}}\right)^{(q)}$ is the rate of change in the cross-sectional area of the martensitic plate when tip q moves. Since the cross-sectional area is $\Omega_k^{\mathrm{m}} = \pi cd = \pi ec^2$, the time rate of the change in area at a constant aspect ratio when tip q moves while the opposite tip is held fixed is

$$\frac{\mathrm{d}}{\mathrm{d}t} \left(\Omega_k^{\mathrm{m}}\right)^{(q)} = \pi ec v_{\mathrm{t}}^{(q)}, \tag{39}$$

where the relation $2\dot{c} = v_{\mathrm{t}}^{(q)}$ was used (see figures 3(*a*) and (*b*)). Equating the dissipation due to the movement of tip q given in (37) to the corresponding dissipation given in (38) and making use of the expression for the rate of change in area (39) provides a relation for the effective driving force $\bar{f}_k^{(q)}$ for each growth mode q, i.e.

$$\bar{f}_k^{(q)} := \frac{1}{\pi ec} \int_{S_k^{\mathrm{m}}} f_k^{\mathrm{tr}} w^{(q)}\, \mathrm{d}s \qquad (q = 1, 2). \tag{40}$$

The transformation is considered to be crystallographically irreversible; hence, the plate is not allowed to change if the driving force is negative. The following effective kinetic relation is proposed for a plate Ω_k^{m}:

$$\frac{\mathrm{d}}{\mathrm{d}t} \left(\Omega_k^{\mathrm{m}}\right)^{(q)} = 0 \qquad \text{if } \bar{f}_k^{(q)} \leqslant 0, \tag{41}$$

$$\frac{\mathrm{d}}{\mathrm{d}t} \left(\Omega_k^{\mathrm{m}}\right)^{(q)} = \frac{\bar{f}_k^{(q)}}{B_{\mathrm{m}}} \qquad \text{if } 0 < \bar{f}_k^{(q)} < \bar{f}_{\max}, \tag{42}$$

$$\frac{\mathrm{d}}{\mathrm{d}t} \left(\Omega_k^{\mathrm{m}}\right)^{(q)} = \dot{\Omega}_{\max} \qquad \text{if } \bar{f}_k^{(q)} \geqslant \bar{f}_{\max}, \tag{43}$$

where B_{m} is a (positive) drag coefficient and $\dot{\Omega}_{\max}$ is the maximum rate of growth, for driving forces exceeding the value $\bar{f}_{\max} = B_{\mathrm{m}}\dot{\Omega}_{\max}$. The dissipation given in (38), making use of kinetic relation (42), is

$$\mathcal{D}_k^{(q)} = B_{\mathrm{m}} \left(\frac{\mathrm{d}}{\mathrm{d}t} \left(\Omega_k^{\mathrm{m}}\right)^{(q)} \right)^2 > 0\,, \tag{44}$$

which indicates that the kinetic relation is consistent with the second law of thermodynamics. If growth occurs at the maximum rate $\dot{\Omega}_{\max}$, then the dissipation is also positive and if no growth occurs, then the dissipation is trivially zero.

Relations (38) and (40) together with the effective kinetic relation (42) yield the following constitutive expression for the tip velocities:

$$v_{\mathrm{t}}^{(q)} = \frac{1}{B_{\mathrm{m}}\, (\pi ec)^2} \int_{S_k^{\mathrm{m}}} f_k^{\mathrm{tr}} w^{(q)}\, \mathrm{d}s \qquad (q = 1, 2). \tag{45}$$

Although $w^{(1)}$ and $w^{(2)}$ are mirror images of each other, the tip velocities $v_{\mathrm{t}}^{(q)}$ are in general different from each other since the local driving force f_k^{tr} does not need to be symmetric with respect to the minor semi-axis of the elliptical plate. For the implementation of the method, the tip velocities are determined from (45), where the integral on the right-hand side can be evaluated numerically for each martensitic platelet.

In the general case both tips are allowed to move *simultaneously*, as shown in figure 3(*c*). In that case, the rate of change in area is equal to $\pi ec(v_{\mathrm{t}}^{(1)} + v_{\mathrm{t}}^{(2)}) = (\mathrm{d}/\mathrm{d}t)\left(\Omega_k^{\mathrm{m}}\right)^{(1)} +$

$(\mathrm{d}/\mathrm{d}t)\left(\Omega_k^{\mathrm{m}}\right)^{(2)}$. However, since the interface normal velocity V_{n} depends non-linearly on the tip velocities when these are simultaneously moving, the total dissipation $\mathcal{D}_k$ is not exactly equal to the sum of the dissipations $\mathcal{D}_k^{(1)}$ and $\mathcal{D}_k^{(2)}$ associated with the individual movement of one tip while the opposite is fixed. In general, the determination of the total dissipation requires the solution of a nonlinear problem. Nevertheless, the approximation $\mathcal{D}_k \approx \mathcal{D}_k^{(1)} + \mathcal{D}_k^{(2)}$ for the total dissipation is relatively accurate since the weighting functions $w^{(q)}$ rapidly decay to zero away from the tips; hence, the total dissipation depends mostly on the local dissipation at each tip q (i.e. $f_k^{\mathrm{tr}} v_t^{(q)}$) which is the same as in the case when both tips move simultaneously (see figure 3).

The maximum growth rate condition (43) for the whole plate can be prescribed by a cut-off value $v_{\max}^{\mathrm{m}}$ for each tip velocity separately, i.e. the following constraint is enforced:

$$0 \leqslant v_{\mathrm{t}}^{(q)} \leqslant v_{\max}^{\mathrm{m}} = \frac{\dot{\Omega}_{\max}}{\pi e c} \qquad (q = 1, 2). \tag{46}$$

Since the length c varies as the plate growths, the maximum growth rate $\dot{\Omega}_{\max}$ is assumed to vary linearly with c such that the maximum velocity $v_{\max}^{\mathrm{m}}$, a physically more meaningful quantity, is taken as a constant parameter. To complete the growth model, additional rules are used to handle special situations. In particular, if one martensitic plate encounters another plate, a free end or a constrained part of the crystal (e.g. a grain boundary or part of the external boundary where displacements are prescribed), the movement of the plate is limited up to the intersection point. Coalescence of two plates occurs if the following conditions are met: (i) the crystallographic transformation system associated with each plate is the same and (ii) due to rapid growth, the new domain occupied by one plate (as predicted by the kinetic law) entirely occupies the new domain occupied by the second plate. In such a case, the smaller martensitic plate is merged with the larger one.

3.3. Discrete dislocation model

The plastic flow that arises due to the nucleation and motion of dislocations is modeled using the discrete dislocation plasticity in [16], with additional constitutive rules to account for the phase transformation. The main ingredients of the model are as follows: in a two-dimensional plane-strain analysis, dislocations are modeled as line singularities in an elastic homogeneous medium. Dislocation loops are modeled as edge dipoles in the plane of deformation. Edge dislocations are restricted to glide in their slip planes along a slip direction. For a dislocation i, with $i = 1, \ldots, N^{\mathrm{d}}$, the slip plane and direction are characterized, respectively, by the slip plane normal $\boldsymbol{n}_i$ and the Burgers vector $\boldsymbol{b}_i$. All Burgers vectors $\boldsymbol{b}_i$ have a magnitude $b \equiv b_i = \boldsymbol{b}_i \cdot \boldsymbol{n}_i$ (no sum on i).

The glide motion of a dislocation i is determined by the Peach–Koehler force, f_i^{d}, which is the change in the potential energy of the body Ω associated with an infinitesimal variation of dislocation position in the glide plane [16]. Hence, f_i^{d} is the shear component of the total stress at the current location of the dislocation (excluding the singular stress field $\boldsymbol{\sigma}_i^{\mathrm{d}}$ of the dislocation i itself), resolved on the slip system $\{\boldsymbol{b}_i, \boldsymbol{n}_i\}$, i.e.

$$f_i^{\mathrm{d}} := \left(\boldsymbol{\sigma} - \boldsymbol{\sigma}_i^{\mathrm{d}}\right) \cdot (\boldsymbol{b}_i \otimes \boldsymbol{n}_i)\ . \tag{47}$$

The nucleation of dislocations is modeled by two-dimensional Frank–Read sources, each of which is a point source on a slip plane. A dislocation dipole is nucleated when the magnitude $|f_i^{\mathrm{d}}|$ of the Peach–Koehler force at the location of source i exceeds a critical value f_i^{cr} during a prescribed time interval t_{nuc}, i.e.

$$\frac{1}{t_{\mathrm{nuc}}} \int_t^{t+t_{\mathrm{nuc}}} |f_i^{\mathrm{d}}|\, \mathrm{d}t \geqslant f_i^{\mathrm{cr}} =: b\tau_i^{\mathrm{cr}}. \tag{48}$$

Here, τ_i^{cr} is a critical resolved shear stress at source i. The dislocation cores are nucleated at a distance L_{nuc} given by

$$L_{nuc} = \frac{\mu}{2\pi(1-\nu)} \frac{b}{\tau_i^{cr}}, \tag{49}$$

where $\mu(=\mu^a)$ is the shear modulus and ν Poisson's ratio of the austenite. This nucleation distance is specified such that the shear stress of one dislocation acting on the other is balanced by the slip plane shear stress. In contrast to transformation sources, dislocation sources are related to a unique slip system and, after nucleation, they remain active to possibly nucleate subsequent dislocation dipoles. The kinetic relation for the dislocation glide is written in the form

$$v_i^d = \frac{f_i^d}{B_d}, \qquad 0 \leqslant v_i^d \leqslant v_{max}^d , \tag{50}$$

where v_i^d is the velocity of the ith dislocation core along the slip direction, B_d is a drag coefficient and v_{max}^d is a cut-off value for the dislocation velocity. In addition, two dislocations of opposite signs are annihilated if their distance is less than $6b_i$. More details can be found in [16].

In order to take into account the elastic behavior of the martensitic plates (see section 2.3), the discrete dislocation model is augmented with the following constitutive rules: (i) dislocations that appeared in the austenitic phase are inherited in the martensitic phase but become immobile, (ii) no new dislocations nucleate in the martensitic regions, i.e. dislocation sources that become part of a martensitic region are de-activated, and (iii) the austenite–martensite interface acts as an impenetrable barrier for mobile dislocations gliding in the austenitic phase. Using the constitutive rules indicated in this section, the configuration of the sample is updated for time $t + \Delta t$ (based on the stress state at time t) and a new equilibrium state for time $t + \Delta t$ is computed using the method outlined in section 2.

4. Single crystal simulations

To illustrate the basic features of the model, simulations of single crystal specimens under uniaxial and biaxial deformations are presented. In order to study the strengthening due to the martensitic transformation, other mechanisms are suppressed from the simulations and, in particular, the specimens contain no dislocation obstacles except for habit planes that appear during the simulation and constrained external boundaries. For all simulations, plane-strain conditions are assumed in the $(1\,1\,0)_a$ plane and two slip systems are considered, which are meant to represent the movement of edge dislocations in the $(\bar{1}\,1\,1)_a$ and $(1\,\bar{1}\,1)_a$ planes in an FCC lattice [20]. These slip plane normals are perpendicular to the out of plane direction $[1\,1\,0]_a$ and form an angle of approximately 60° between them. As mentioned in section 2.2.1, none of the actual 24 transformation systems found in an FCC to BCT transformation are compatible with plane-strain conditions (i.e. none of the habit plane vectors are perpendicular to the $[1\,1\,0]_a$ direction). However, for consistency with plane-strain conditions in the $(1\,1\,0)_a$ plane, the transformation systems used in the simulations are taken such that the habit plane normal vectors $\boldsymbol{m}_k$ and the shape strain vectors $\boldsymbol{a}_k$ are perpendicular to the $[1\,1\,0]_a$ direction. In particular, two crystallographically distinct habit plane normal vectors are chosen oriented at angles of 40° and 80° with respect to the slip plane normals. These angles are chosen to mimic the actual three-dimensional angles between slip planes and habit planes, which vary between 27° and 153° in a high-carbon FCC austenitic lattice. Dislocation sources are randomly distributed on slip planes spaced $200b$ apart and each source is randomly assigned a nucleation

Table 1. Parameters for the transformation–dislocation model.

Parameter(s)	Value(s)	Equation(s)
Elastic moduli		
Austenite	$\kappa^{a} = 150\,\text{GPa}$, $\mu^{a} = 69.2\,\text{GPa}$	(9)
Martensite	$\kappa^{m} = 195\,\text{GPa}$, $\mu^{m} = 90\,\text{GPa}$	(9)
Transformation		
Strain	$\delta = 4 \times 10^{-3}$, $\gamma = 2 \times 10^{-2}$	(8)
Source strength	f_k^{cr} (Gaussian) mean $= 4\,\text{MPa}$, Std.dev. $= 0.8\,\text{MPa}$	(34)
Embryonic plate	$c_0 = 0.1\,\mu\text{m}$, $e = 0.125$	(45)
Kinetic law	$B_m = 10^8\,\text{Pa s m}^{-2}$, $\upsilon_{max}^{m} = 4800\,\text{m s}^{-1}$	(45), (46)
Dislocation		
Burgers vector	$b = 0.25\,\text{nm}$	(47),(48)
Source strength	τ_i^{cr} (Gaussian) mean $= 170\,\text{MPa}$, Std.dev. $= 34\,\text{MPa}$	(48)
	$t^{nuc} = 10\,\text{ns}$	
Kinetic law	$B_d = 10^{-4}\,\text{Pa s}$, $\upsilon_{max}^{d} = 20\,\text{m s}^{-1}$	(50)

strength from a Gaussian distribution. The dislocation source density is approximately $20\,\mu\text{m}^{-2}$. The location and strength of the transformation sources are distributed in similar ways, with a density (per unit depth) of approximately $8\,\mu\text{m}^{-2}$. The initial configuration of the specimens for all simulations corresponds to a stress-free, dislocation-free and fully austenitic state.

4.1. Transformation and dislocation systems and material parameters

The material parameters for the transformation–dislocation model are shown in table 1. The stiffness of the martensitic phase is taken 30% higher than that of the austenitic phase, and the values are representative for phases in carbon steels [11]. The parameters for the transformation strain are chosen as *scaled* values of the actual crystallographic values typical of high-carbon retained austenite [11] (scaled by a factor of 0.1). The purpose of this scaling is to obtain representative stress values while keeping the number of dislocations within a computationally tractable range. Although the simulations are carried out under quasi-static conditions (hence, nominally, the sound speed is infinite), the maximum transformation velocity is set equal close to the actual sound speed of the austenitic phase. The size of the embryonic plate c_0 is chosen such that the density of martensitic twins is large enough to use (8) as a representative transformation strain. The dislocation strength is calibrated to provide a representative initial yield strength for the austenitic phase, while the transformation strength is based on typical effective critical values for multiphase steels [11]. The transformation drag coefficient is estimated by relating representative values of the driving force and the tip velocity. The representative driving force is computed based on the mean critical value for the nucleation driving force f_k^{cr} acting on an embryonic plate without dislocations and the corresponding tip velocity is set at a fraction of the sound speed.

4.2. Uniaxial extension and contraction

In this section, a rectangular specimen with in-plane dimensions $L = 12\,\mu\text{m}$ and $h = 4\,\mu\text{m}$, as shown in figure 4, is subjected to plane-strain uniaxial deformation by imposing the following

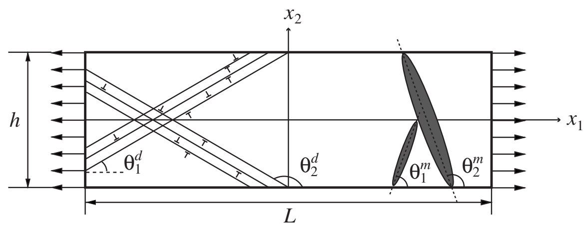

Figure 4. Schematic illustration of the specimen.

Table 2. Orientations A and B: slip planes and (unconstrained) habit planes (see figure 4).

Orientation	$\theta_1^{\rm d}$	$\theta_2^{\rm d}$	$\theta_1^{\rm m}$	$\theta_2^{\rm m}$
A	30°	150°	70°	110°
B	340°	100°	20°	60°

boundary conditions:

$$u_1(x_1 = \pm L/2, t) = \pm\tfrac{1}{2}L\dot{\varepsilon}t, \qquad u_2(x_1 = \pm L/2, t) = 0, \tag{51}$$

$$\sigma_{12}(x_2 = \pm h/2, t) = 0\ , \qquad \sigma_{22}(x_2 = \pm h/2, t) = 0, \tag{52}$$

with a nominal strain rate $\dot{\varepsilon} = \pm(1/6) \times 10^4\,\mu\mathrm{m\,s}^{-1}$ for extension and compression, respectively. The left and right sides of the specimen ($x_1 = \pm L/2$) are taken to be impenetrable boundaries for dislocations in order to satisfy the applied displacements according to (51). The top and bottom sides ($x_2 = \pm h/2$) are traction-free; hence, dislocations can exit from these boundaries and form a step.

Two crystal orientations are analyzed in this section, referred to as orientations A and B, as indicated in table 2. For orientation A the slip systems are oriented symmetrically with respect to the loading direction while orientation B is obtained as a 50° clockwise rotation of orientation A. For each crystal orientation, three simulations are performed: (1) a simulation where the dislocation mechanism is suppressed; (2) one where the transformation mechanism is not taken into account and (3) a coupled dislocation–transformation simulation. The benchmark cases 1 and 2 are used in conjunction with the general case 3 to investigate the interaction between plastic flow and phase transformation.

The stress–strain responses for orientations A and B are shown in figures 5(*a*) and (*b*), respectively, where in each case the results are given for configurations 1, 2 and 3. The stress–strain responses are presented in terms of the average axial stress $\bar{\sigma}_{11}$ as a function of the average axial strain $\bar{\varepsilon}_{11} := \dot{\varepsilon}t$. The onset of transformation for configuration 1 and the onset of plastic slip for configuration 2 are indicated by arrows in figures 5(*a*) and (*b*).

For both orientations A and B, the response to extension for the transformation-only configuration 1 is characterized by sudden reductions in stress as platelets of martensite nucleate and grow. Each discrete stress relaxation event is followed by an elastic stress build-up until new platelets of martensite nucleate. The remaining transformation sources need to be activated at a higher average stress. The net effect of this sequence of events is characterized by a significant hardening as the transformation proceeds and eventually the average stress actually increases with the nucleation of new platelets. Under uniaxial compression, the response of the specimen with orientation A and configuration 1 shown in figure 5(*a*) is purely elastic since the martensitic systems are not favorably oriented for transformation under uniaxial compression, giving a negative driving force. In contrast, the specimen with orientation B

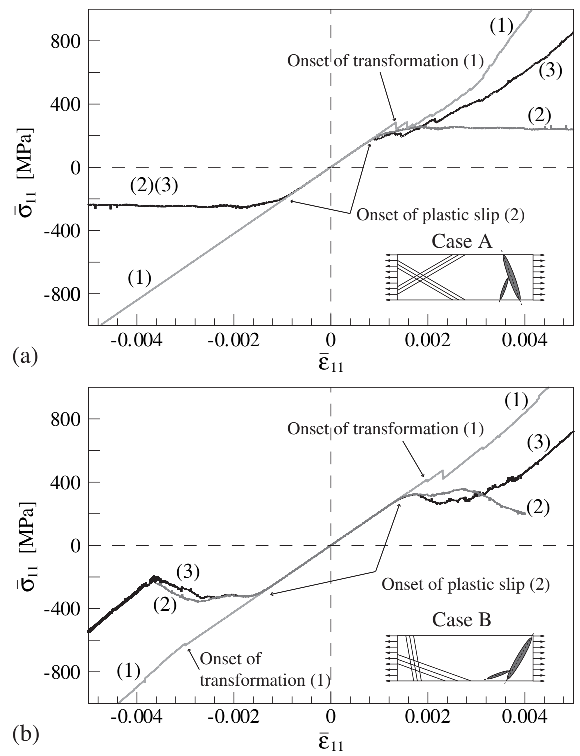

Figure 5. Average axial stress $\bar{\sigma}_{11}$ versus average axial strain $\bar{\varepsilon}_{11}$ for (*a*) orientation A and (*b*) orientation B. Each case includes the following configurations: (1) transformation sources only, (2) dislocation sources only and (3) transformation and dislocation sources.

and configuration 1 has one martensitic system favorably oriented under compression and transformation is observed (see figure 5(*b*)).

For both orientations, the tensile and compressive responses for the case of dislocations only (configuration 2) are identical, apart from the sign. The initial elastic deformation is followed by a plateau-type response typical of a simulation without internal obstacles (i.e. no hardening). The stress level at which the plateau begins is higher for orientation B than for orientation A, which is consistent with the Schmid factors under homogeneous uniaxial stress states. The stress–strain curve for orientation B is shown only up to a limited strain level. For higher strains (and also for orientation A), the predictions with dislocations only give rise to a strong softening. This softening is an artifact mainly due to a localization of deformation connected to the specimen's grips, which act as impenetrable barriers for dislocations.

Comparing curves 1 and 2 in figure 5, it can be seen that the average stress at which the transformation starts is higher than that when dislocations are generated. Consequently, for the coupled transformation–dislocation case (configuration 3), the onset of the inelastic response is controlled by plastic slip. For orientation A in compression, the curve for configuration 3 is identical to that of configuration 2 (dislocation-only case) since there is no transformation. For orientation A in tension, the simulations indicate that the transformation mechanism is activated shortly after the onset of plastic deformation at an average stress level well below that of configuration 1 (i.e. transformation-only case). In this case, transformation sources are activated by a locally high stress associated with dislocations. The axial stress for the combined transformation–dislocation case (curve 3 in figure 5(*a*)) lies initially below the dislocation-only curve 2, suggesting that a combination of transformation and plastic slip is more efficient in relaxing the stress than by plastic deformation only. Nevertheless, as the strain level is increased, the dislocation-only case provides the largest stress relaxation (i.e. curve 2 lies below curve 3 for larger strains) while the response of the coupled transformation–dislocation configuration follows a hardening behavior similar to that of configuration 1.

The most favorable inelastic mechanism is typically the one that provides the largest decrease in energy (e.g. more stress relaxation). According to the results of the simulations, at the end of the loading program, the largest relaxation can be achieved by plastic deformation alone (i.e. without transformation), as the stress–strain curves of configuration 3 show in figure 5. Although the transformation releases energy, it increases the strength of the material eventually. Notwithstanding the long term benefit of plastic deformation alone, transformation is also activated in the coupled case due to the fact that (i) the combined effect of plasticity and transformation is to provide the *largest* relaxation at a given *instant* and (ii) the activation of relaxation mechanisms is *independent* of the behavior at *subsequent* strains (i.e. the current response of the material is independent of its future behavior).

For orientation B, see figure 5(*b*), the coupled stress–strain curves in tension and compression are qualitatively similar to that of orientation A in tension. In particular, the transformation mechanism in configuration 3 is activated shortly after the onset of plastic deformation and the strength of the material falls below that of the dislocation-only case. This trend continues for a longer strain range for orientation B than for orientation A. Eventually, however, the hardening behavior of configuration 3 becomes similar to that of configuration 1 and the strength of the coupled case becomes higher than that of the dislocation-only configuration. Hence, for both orientations, the effect of the phase transformation is to eventually strengthen the material.

The martensitic volume fraction ξ^{m} as a function of the average axial strain $\bar{\varepsilon}_{11}$ is shown in figures 6(*a*) and (*b*) for orientation cases A and B, respectively, and, in each case, for configurations 1 and 3 (i.e. without and with plastic deformation, respectively). The volume fraction is computed as

$$\xi^{\mathrm{m}} := \frac{1}{\Omega} \sum_{k=1}^{N^{\mathrm{m}}} \Omega_k^{\mathrm{m}}, \tag{53}$$

where Ω_k^{m} refers in this expression to the volume (area per unit depth) of the martensitic plate k. Comparing the responses of configurations 1 and 3 shown in figure 6 it can be observed that the effect of plastic flow is to lower the average strain (and stress) at which transformation initially occurs. In general, the appearance of martensitic platelets occurs soon after plastic flow is initiated. However, as the deformation proceeds, the number of martensitic plates in the specimen is generally lower for the coupled case (configuration 3) than for the transformation-only case (configuration 1), which indicates that the effect of plastic slip is to reduce the transformation rate.

The density of dislocations $\rho^{\mathrm{d}} := N^{\mathrm{d}}/\Omega$ as a function of the average axial strain $\bar{\varepsilon}_{11}$ is shown in figures 7(*a*) and (*b*) for orientation cases A and B, respectively and, in each case, for configurations 2 and 3 (i.e. without and with phase transformation, respectively). The dislocation density includes the dislocations in the martensitic regions that have become immobile.

Comparing the responses of configurations 2 and 3 shown in figure 7 it can be observed that the net amount of dislocations is substantially higher due to the phase transformation in uniaxial tension (for both orientations) and in uniaxial compression for orientation B. For orientation A in compression, the dislocation density is the same for configurations 2 and 3 since there is no transformation.

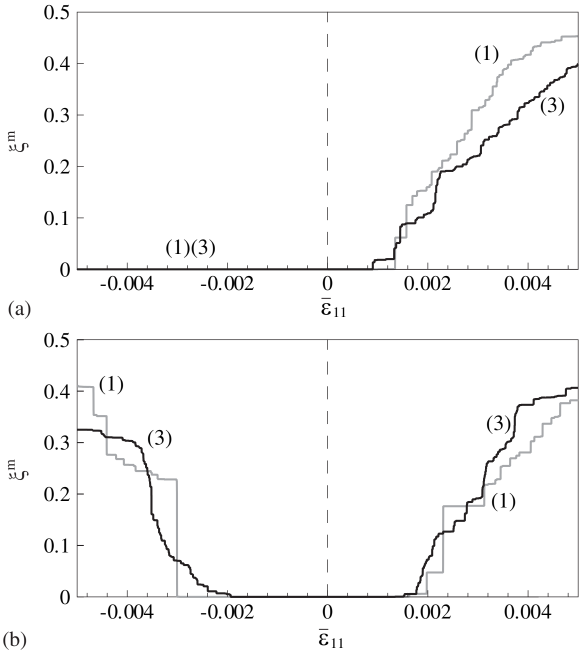

Figure 6. Martensitic volume fraction ξ^{m} versus average axial strain $\bar{\varepsilon}_{11}$ for (*a*) orientation A and (*b*) orientation B. Each case includes the following configurations (1) transformation sources only and (3) transformation and dislocation sources.

To gain more insight into the detailed interaction between phase transformation and plastic flow, the spatial distributions of dislocations, martensitic plates and the axial stress σ_{11} are shown in figure 8 for orientation A. The martensitic plates are represented by elliptical plates and the dislocations are represented by '+' and '−' symbols corresponding to positive and negative dislocations, with the colors indicating the slip system (black for system 1 and white for system 2).

The plot for the transformation-only case for orientation A shown in figure 8(*a*) indicates that both transformation systems are approximately evenly active, forming a pattern where platelets of the same system tend to be clustered. In the plot for the dislocation-only case shown in figure 8(*b*), it can be observed that several dislocation pile-ups have developed due to the constrained grips, although some internal pile-ups appear due to the constraining effect of dislocations in other slip systems. A comparision of the transformation-only case (configuration 1) and the coupled transformation–dislocation case (configuration 3 shown in figure 8(*c*)) reveals some interesting points regarding the effect of the plastic deformation on transformation. It can observed that, as for the transformation-only case, both transformation systems are active in the coupled case, although the plastic deformation tends to limit the growth of individual plates. The plates occupy less volume and are less clustered than in the transformation-only case. A comparision of the dislocation-only case (configuration 2) and the coupled transformation–dislocation case (configuration 3) shows that the effect of the transformation on plastic deformation is to increase the number of dislocations despite the reduction of dislocation sources (the dislocation sources trapped in the martensitic plates become inactive). The remaining sources nucleate more dislocations than in the dislocation-only case, particularly those that are close to martensitic plate tips. In addition, dislocations

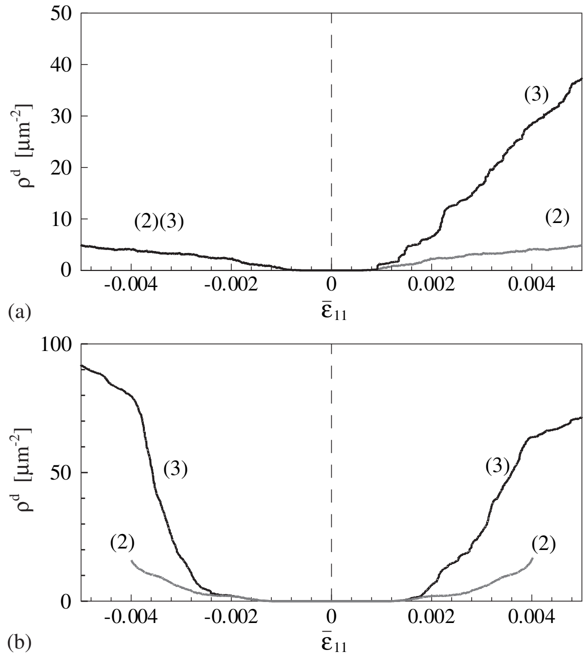

Figure 7. Dislocation density ρ^{d} versus average axial strain $\bar{\varepsilon}_{11}$ for (*a*) orientation A and (*b*) orientation B. Each case includes the following configurations (2) dislocation sources only and (3) transformation and dislocation sources.

are prevented from escaping the specimen due to the restraining effect of the martensitic plates; hence, the dislocation density remains higher than in the dislocation-only case.

In the dislocation–transformation configuration, discrete dislocations are generated first and, due to the local modification of the stress field, they trigger the nucleation of martensitic plates. In turn, more dislocations are generated due to the transformation and the process continues with a strong coupling between these two phenomena. Moreover, dislocation pile-ups are visible between martensitic plates, which indicates a hardening effect related to a reduction in the effective austenitic grain size (an effect that can be thought of as an 'evolving' Hall–Petch effect). In addition, the increase in strength is related to the higher stiffness of the product martensitic phase.

For orientation B, the spatial distributions of dislocations, martensitic plates and the axial stress σ_{11} under uniaxial extension are shown in figure 9 at an average strain level $\bar{\varepsilon}_{11} = 0.4\%$. Figure 9(*a*) for the transformation-only case reveals that only a single transformation system (system 1) is active and that the transformation region is somewhat localized. The simulation results for dislocations only, as observed in figure 9(*b*), are qualitatively similar to those of orientation A in the sense that pile-ups appear at the constrained ends of the specimen as well as internal pile-ups due to the stress field generated by dislocations in neighboring slip planes. The coupled transformation–dislocation case presented in figure 9(*c*) shows that *both* transformation systems are active under uniaxial extension (although system 1 remains the preferentially activated system). In view of the stress distributions for configurations 1 and 3, it can be seen that one effect of the plastic deformation is to modify the stress field locally such that the transformation system 2 also becomes active. Similar to the case of orientation A, dislocation pile-ups are visible between martensitic plates in figure 9(*c*).

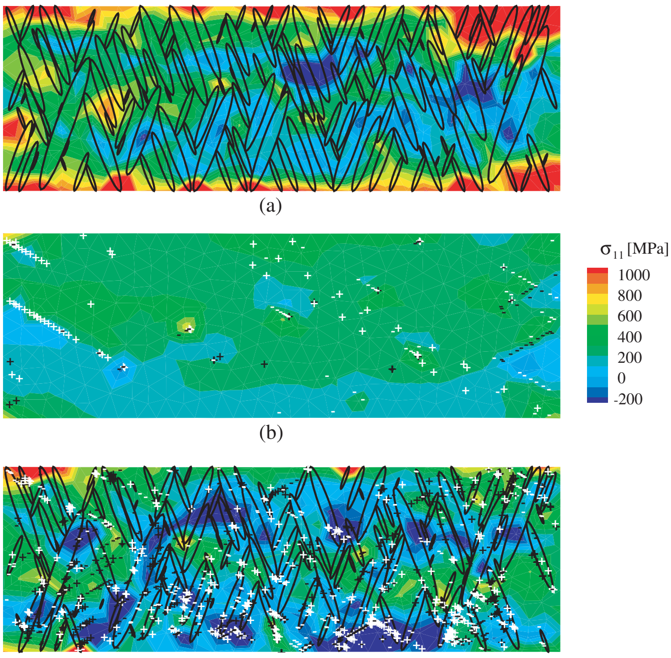

Figure 8. Distribution of axial stress σ_{11} and distribution of dislocations and martensitic plates when $\bar{\varepsilon}_{11} = 0.42\%$ for orientation A and (*a*) transformation sources only, (*b*) dislocation sources only and (*c*) transformation and dislocation sources.

4.3. Loading/unloading cycle

Displacement-controlled simulations of a loading/unloading cycle were carried out to gain further insight into the coupling between plastic flow and transformation. To this end, the strain rate appearing in (51) is taken to have the value $\dot{\varepsilon} = (1/6) \times 10^4\,\mu\mathrm{m\,s^{-1}}$ for $0 \leqslant t \leqslant T/2$ and $-(1/6) \times 10^4\,\mu\mathrm{m\,s^{-1}}$ for $T/2 \leqslant t \leqslant T$. The time T is chosen such that the axial strain at time $T/2$ is 0.28%.

The stress–strain response, given in terms of the average axial stress $\bar{\sigma}_{11}$ as a function of the average axial strain $\bar{\varepsilon}_{11}$, is shown in figure 10 for the transformation-only case (configuration 1), the plasticity-only case (configuration 2) and the coupled transformation–dislocation case (configuration 3). The unloading part of the stress–strain curves is indicated with an asterisk next to the configuration number. The dashed vertical line indicates the strain at which the displacement is reversed from extension to contraction (same strain for all cases). In order to analyze the stress–strain responses, it is useful to refer to the evolutions of the martensitic volume fraction ξ^{m} and the density of dislocations ρ^{d} as functions of the average axial strain $\bar{\varepsilon}_{11}$, which are shown in figures 11(*a*) and (*b*), respectively.

The transformation-only case (configuration 1) unloads elastically (see figure 11(*a*)) and the additional effective elastic stiffness gained due to the appearance of a stiffer martensitic phase is evidenced from the higher slope in the unloading curve shown in figure 10 (compared with the elastic loading portion). For the plasticity-only case (configuration 2) new dislocation dipoles that nucleate during unloading are subsequently annihilated since the dislocations attract each other as the load is further reduced. From this point of view, the unloading stage can be characterized as being elastic. The reduction in the dislocation density (shown

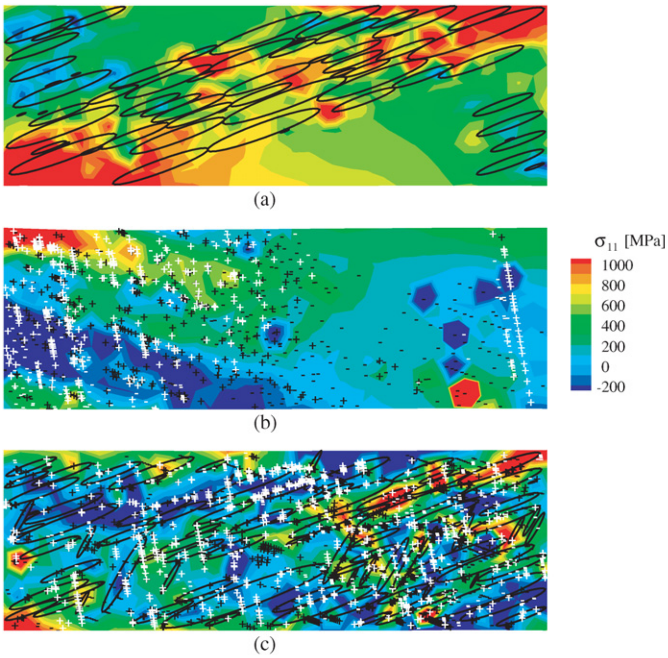

Figure 9. Distribution of axial stress σ_{11} and distribution of dislocations and martensitic plates when $\bar{\varepsilon}_{11} = 0.42\%$ for orientation B and (*a*) transformation sources only, (*b*) dislocation sources only and (*c*) transformation and dislocation sources.

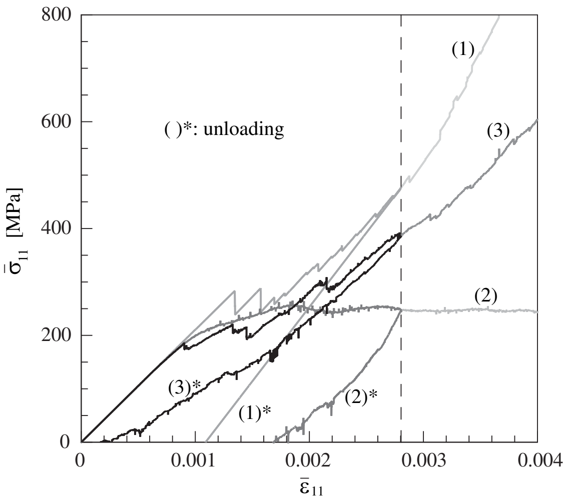

Figure 10. Average axial stress $\bar{\sigma}_{11}$ versus average axial strain $\bar{\varepsilon}_{11}$ for orientation A and cases (1) transformation sources only, (2) dislocation sources only and (3) transformation and dislocation sources. The asterisk in the corresponding case number indicates the evolution during unloading.

in figure 11(*b*)) is related to dislocations that exit the domain through the free boundaries of the domain (top and bottom surfaces). For the coupled case (configuration 3), limited transformation is observed during unloading (see figure 11(*a*)) but, interestingly, the dislocation density increases substantially during unloading (see figure 11(*b*)). This behavior can be

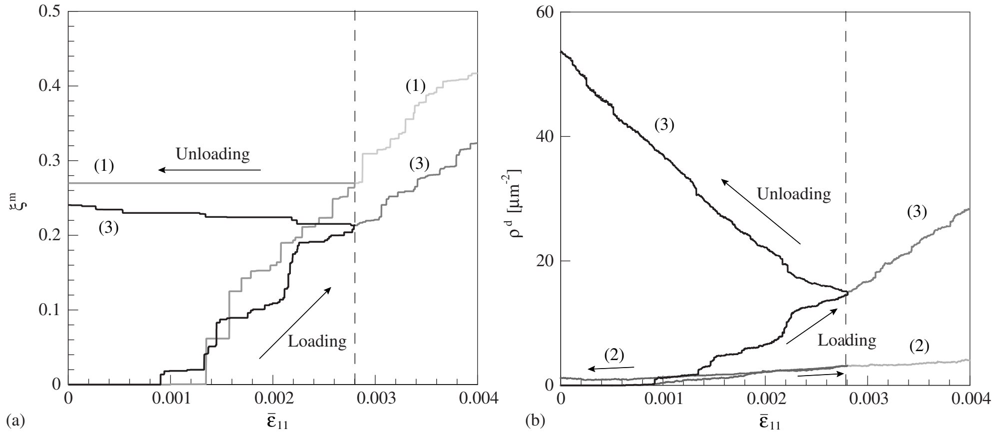

Figure 11. (*a*) Martensitic volume fraction ξ^m versus average axial strain $\bar{\varepsilon}_{11}$ for orientation A and for cases (1) transformation sources only and (3) transformation and dislocation sources; (*b*) Dislocation density ρ^d versus average axial strain $\bar{\varepsilon}_{11}$ for orientation A and cases (2) dislocation sources only and (3) transformation and dislocation sources.

traced back to the following: (i) during transformation, martensitic platelets nucleate in the specimen and obstruct the path of dislocations towards the free boundaries. In this case, dislocations pile up at habit planes and (ii) although the *average* stress is reduced during unloading, significant stress concentrations remain in the specimen, which keep the dislocation sources active throughout the process.

5. Concluding remarks

Despite the limitations of a two-dimensional framework, the present discrete dislocation–transformation model provides useful information regarding the complex interaction between plastic slip and martensitic phase transformations. The simulations for a single crystal of austenite under uniaxial deformation indicate that instantaneously the most efficient mechanism for stress relaxation can be achieved by a combination of transformation and plastic deformation. However, these mechanisms are quickly depleted and the material experiences a strong hardening. The appearance of hard martensitic plates that cannot deform plastically increases the overall strength, reduces the number of dislocation sources and generates multiple barriers for dislocations. The subdivision of the austenitic grain by martensitic platelets reduces the effective austenitic grain and creates a pronounced Hall–Petch effect. In general, plastic slip reduces the average stress at which transformation begins but eventually reduces the transformation rate under uniaxial deformation. Furthermore, local stress fluctuations caused by dislocations can activate transformation systems that *a priori* would not appear to be favorable based on the average stress.

In contrast to a purely elasto-plastic behavior, the discrete elasto-plastic-transformation model predicts plastic deformations during unloading, with a significant increase in dislocation density. This information is relevant for the development of meso- and macroscopic theories of transformation-induced plasticity. In particular, theories based on a stress that represents an average over the austenitic and martensitic phases would not be able to predict the activation of secondary transformation systems, which suggests that secondary activations have to be included phenomenologically. Furthermore, a macroscopic model for plastic deformation would need to take into account a size effect formally similar to an evolving Hall–Petch relation, where the grain size is reduced as the transformation proceeds. Accordingly, the calibration of a plastic model in a macroscopic model cannot be based on a purely austenitic plastic behavior.

Acknowledgments

This research was carried out under the project number MC2.03177 in the framework of the Research Program of the Materials innovation institute M2i (www.m2i.nl), the former Netherlands Institute for Metals Research.

Appendix A. Solution to void problem

Consider an infinite homogeneous and isotropic medium with a traction-free elliptical void with semi-axes c and d centered at the origin of coordinates. Let x_1 and x_2 be Cartesian coordinates along directions aligned with the principal directions of the ellipse and let κ^{a} and μ^{a} be the bulk and shear moduli of the medium. The infinite domain is subjected to a remote uniaxial stress field characterized by a loading σ_∞ applied in a direction that forms an angle θ with respect to the x_1-axis. Mushkelishvili's potentials used to solve this problem are given by (see, e.g. [26])

$$\varphi(\zeta) = \frac{\sigma_\infty R}{4}\left(\frac{1}{\zeta} + \left[2\mathrm{e}^{2\mathrm{i}\theta} - m\right]\zeta\right),$$
$$\psi(\zeta) = -\frac{\sigma_\infty R}{2}\left(\frac{1}{\zeta}\mathrm{e}^{-2\mathrm{i}\theta} + \frac{\left[1 - m\mathrm{e}^{2\mathrm{i}\theta} + m^2\right]\zeta - \mathrm{e}^{2\mathrm{i}\theta}\zeta^3}{1 - m\zeta^2}\right), \tag{A.1}$$

where $R = (c+d)/2$, $m = (c-d)/(c+d)$, $i^2 = -1$ and ζ is a complex variable in a domain where the ellipse has been transformed into a circle of radius R. The components of the stress field $\boldsymbol{\sigma}^{\mathrm{v}}$ and the displacement field $\boldsymbol{u}^{\mathrm{v}}$ in the Cartesian coordinate system x_1, x_2 can be computed as

$$\sigma^{\mathrm{v}}_{22} + \sigma^{\mathrm{v}}_{11} = 4\mathrm{Re}\varphi_*{}'(z),$$
$$\sigma^{\mathrm{v}}_{22} - \sigma^{\mathrm{v}}_{11} + 2\mathrm{i}\sigma^{\mathrm{v}}_{12} = 2\left[\bar{z}\varphi_*{}''(z) + \psi_*{}'(z)\right], \tag{A.2}$$
$$2\mu^{\mathrm{a}}(u^{\mathrm{v}}_1 + \mathrm{i}u^{\mathrm{v}}_2) = \left(\frac{3\kappa^{\mathrm{a}} + 7\mu^{\mathrm{a}}}{3\kappa^{\mathrm{a}} + \mu^{\mathrm{a}}}\right)\varphi_*(z) - z\overline{\varphi_*{}'(z)} - \overline{\psi_*{}'(z)},$$

where $z = x_1 + \mathrm{i}x_2$, Re refers to the real part, an overbar indicates the complex conjugate, $()'$ stands to $\mathrm{d}/\mathrm{d}z$ and φ_* and ψ_* are Mushkelishvili's potentials expressed in terms of the complex variable z in the original domain [26]. To solve this problem, one has to use a mapping to transform a circle into an ellipse, i.e.

$$\zeta^{\pm}(z) = \frac{z \pm \sqrt{z^2 - 4mR^2}}{2mR}, \tag{A.3}$$

where $\zeta^{\pm}$ refers to the two branches of mapping, which generate two sets of functions, namely, $\varphi^{\pm}_*(z) = \varphi(\zeta^{\pm}(z))$ and $\psi^{\pm}_*(z) = \psi(\zeta^{\pm}(z))$. Inserting (A.3) in (A.1) and solving (A.2) provide expressions for the stress and displacement components. Care must be exercised when choosing the appropriate branch (i.e. either ζ^+ or ζ^-) for each part of the domain.

It is noted that, since Mushkelishvili's potentials provide the solution only for uniaxial loading, to obtain the actual solution to the void problem under general loading one has to determine the in-plane principal stresses and directions of $-\boldsymbol{\sigma}^{\mathrm{b}}$ (as indicated in section 2.2.2), compute the stress and displacements fields separately for each principal stress and use the principle of superposition to determine the total in-plane components of $\boldsymbol{\sigma}^{\mathrm{v}}$ and $\boldsymbol{u}^{\mathrm{v}}$.

References

[1] Sugimoto K I, Mitsuyuki K and Hashimoto S I 1992 Ductility and strain-induced transformation in a high-strength transformation-induced plasticity-aided dual-phase steel *Metall. Trans.* A **23** 3085–91

[2] Sugimoto K I, Kobayashi M and Yasuki S I 1997 Cyclic deformation behavior of a transformation-induced plasticity-aided dual-phase steel *Metall. Mater. Trans.* A **28** 2637–44

[3] Jacques P J, Furnémont Q, Mertens A and Delannay F 2001 On the sources of work hardening in multiphase steels assisted by transformation-induced plasticity *Phil. Mag.* A **81** 1789–812

[4] Jacques P J, Furnémont Q, Godet S, Pardoen T, Conlon K T and Delannay F 2006 Micromechanical characterisation of trip-assisted multiphase steels by *in situ* neutron diffraction *Phil. Mag.* **86** 2371–92

[5] Leblond J B, Mottet G and Devaux J C 1986 A theoretical and numerical approach to the plastic behaviour of steels during phase-transformation—I. Derivation of general relations *J. Mech. Phys. Solids* **34** 395–409

[6] Stringfellow R G, Parks D M and Olson G B 1992 A constitutive model for transformation plasticity accompanying strain-induced martensitic transformations in metastable austenitic steels *Acta Metall. Mater.* **40** 1703–16

[7] Marketz F and Fischer F D 1995 A mesoscale study on the thermodynamic effect of stress on martensitic transformation *Metall. Mater. Trans.* A **26** 267–78

[8] Levitas V I, Idesman A V and Stein E 1999 Shape memory alloys: micromechanical modeling and numerical analysis of structures *J. Intel. Mater. Syst. Struct.* **10** 983–96

[9] Levitas V I, Idesman A V and Olson G B 1998 Continuum modeling of strain-induced martensitic transformation at shear-band intersections *Acta Mater.* **47** 219–33

[10] Idesman A V, Levitas V I and Stein E 1999 Elastoplastic materials with martensitic phase transition and twinning at finite strains: numerical solution with the finite element method *Comput. Methods Appl. Mech. Eng.* **173** 71–98

[11] Turteltaub S and Suiker A S J 2005 Transformation-induced plasticity in ferrous alloys *J. Mech. Phys. Solids* **53** 1747–88

[12] Suiker A S J and Turteltaub S 2005 Computational modelling of plasticity induced by martensitic phase transformations *Int. J. Numer. Meth. Eng.* **63** 1655–93

[13] Turteltaub S and Suiker A S J 2006 A multi-scale thermomechanical model for cubic to tetragonal martensitic phase transformations *Int. J. Solids Struct.* **43** 4509–45

[14] Turteltaub S and Suiker A S J 2006 Grain size effects in multiphase steels assisted by transformation-induced plasticity *Int. J. Solids Struct.* **43** 7322–36

[15] Tjahjanto D D, Turteltaub S, Suiker A S J and van der Zwaag S 2006 Modelling of the effects of grain orientation on transformation-induced plasticity in multiphase steels *Modelling Simul. Mater. Sci. Eng.* **14** 617–36

[16] van der Giessen E and Needleman A 1995 Discrete dislocation plasiticity: a simple planar model *Modelling Simul. Mater. Sci. Eng.* **3** 689–735

[17] Wechsler M S, Lieberman D E and Read T A 1953 On the theory of the formation of martensite *Trans. Am. Inst. Min. Met. Eng.* **197** 1503–15

[18] Ball J M and James R D 1987 Fine phase mixtures as minimizers of energy *Arch. Ration. Mech. Anal.* **100** 13–52

[19] Hane K F and Shield T W 1998 Symmetry and microstructure in martensites *Phil. Mag.* A **78** 1215–52

[20] Rice J R 1987 Tensile crack tip fields in elastic ideally plastic crystals *Mech. Mater.* **6** 317–35

[21] Mura T 1987 *Micromechanics of Defects in Solids* (Dordrecht: Nijhoff) 2nd edn

[22] Bowen P, Druce S G and Knott J F 1986 Effects of microstructure on cleavage fracture in pressure-vessel steel *Acta Metall.* **34** 1121–31

[23] Shyne J C and Nix W D 1965 Dislocations in martensite inherited from austenite *Acta Metall.* **13** 869–70

[24] R. Abeyaratne and Knowles J K 1990 On the driving traction acting on a surface of strain discontinuity in a continuum *J. Mech. Phys. Solids* **38** 345–60

[25] Abeyaratne R and Knowles J K 1991 Kinetic relations and the propagation of phase boundaries in solids. *Arch. Ration. Mech. Anal.* **114** 119–54

[26] Sokolnikoff I S 1956 *Mathematical Theory of Elasticity* (New York: McGraw-Hill)